Internal Transport Barrier on $q=3$ Surface and Poloidal Plasma Spin Up in JT-60U High-β_p Discharges

Y. Koide, M. Kikuchi, M. Mori, S. Tsuji, S. Ishida, N. Asakura, Y. Kamada, T. Nishitani, Y. Kawano, T. Hatae, T. Fujita, T. Fukuda, A. Sakasai, T. Kondoh, R. Yoshino, and Y. Neyatani

Japan Atomic Energy Research Institute, Naka Fusion Research Establishment, Naka-machi, Naka-gun, Ibaraki-ken 311-01, Japan

(Received 27 May 1993)

Spontaneous formation of an internal transport barrier was observed associated with improved confinement in the high-β_p discharges in the JT-60U tokamak. The radial location of the transport barrier was found to be on the $q=3$ surface. A fast magnetohydrodynamic event localized at the transport barrier triggered the subsequent formation of an edge transport barrier that resulted in the further confinement improvement. In these discharges, a high poloidal plasma rotation velocity that significantly exceeded the prediction of the present neoclassical theory was also observed at $r/a=0.8$.

PACS numbers: 52.55.Fa, 52.25.Fi, 52.55.Pi

Tokamak operation in the high-β_p regime is a promising concept for a steady-state tokamak reactor [1,2]. Here the poloidal beta is defined as $\beta_p=2\mu_0\langle p\rangle/B_p^2$, where $\langle p\rangle$ is the volume-averaged plasma pressure and B_p is the averaged poloidal magnetic field on the plasma surface. An energy confinement time, τ_E, more than 2 times that for L mode (for example, ITER89-P [3]) is required in the high-β_p regime to reduce the plasma current for ignition and hence to achieve efficient steady-state tokamak operation [4]. Improved confinement time was observed in the high-β_p regime ($\beta_p=1$-2) in JT-60U where the confinement improvement factor, $\tau_E/\tau_E^{\text{ITER89-P}}$, increased with $\varepsilon\beta_p$ [5]. In this regime, the "high-β_p mode," a bootstrap-current fraction of up to 58% and a central ion temperature, $T_i(0)$, of 38 keV were achieved simultaneously. Recently the high-β_p mode regime was extented to a lower q regime ($q_{\text{eff}}\sim 4.3$; q_{eff} is the effective surface safety factor defined in Ref. [6]) by using current profile control to avoid sawteeth. And high fusion performance was attained in this regime [7,8]. This Letter describes two distinctive features of this high-β_p mode: (1) the formation of an "internal" transport barrier near the $q=3$ rational surface and (2) the appearance of high poloidal plasma rotation velocity of ~ 50 km/s in the plasma interior.

In JT-60U, high-β_p experiments were performed with a lower single-null configuration, in which the ion ∇B drift is directed toward the X point. Major plasma conditions were plasma major radius, R_p, of 3.05 m, plasma minor radius, a_p, of 0.7 m (the aspect ratio, $\varepsilon^{-1}\equiv R_p/a_p$, was 4.4), the ellipticity, κ, of 1.7, and the plasma volume, V_p, of 48 m^3. The plasma current I_p, the toroidal field at the plasma center, B_t, and q_{eff} were varied in ranges of 0.9-2.2 MA, 3.0-4.4 T, and 4.3-10.0, respectively. Near-perpendicular deuterium neutral beams (NB) up to 22 MW and tangential NB up to 8 MW with a beam energy of 90-95 keV were injected into the low target density ($\leq 1\times 10^{19}$ m^{-3}) Ohmic discharges. To obtain a low recycling condition for the graphite walls, boronization [9], and overnight helium glow discharges were carried out. Profiles of ion temperature, T_i, and impurity plasma rotation velocities in toroidal and poloidal directions, V_t and V_p, were measured using charge exchange recombination spectroscopy (CXRS) at the CVI transition (5290.5 Å) every 50 ms. In this Letter, negative V_t and negative V_p correspond to the counterrotation to the plasma current and the poloidal rotation in the ion-diamagnetic direction, respectively.

The evolution of a typical high-β_p discharge is shown in Fig. 1. During the initial phase of NB heating ($t=5.05$-5.55 s), confinement improvement was rather modest ($\tau_E=1.4\times\tau_E^{\text{ITER89-P}}$) while both the n_e and T_i profiles peaked [$n_e(0)/\langle n_e\rangle$ to 3.7 and $T_i(0)/\langle T_i\rangle$ to 5].

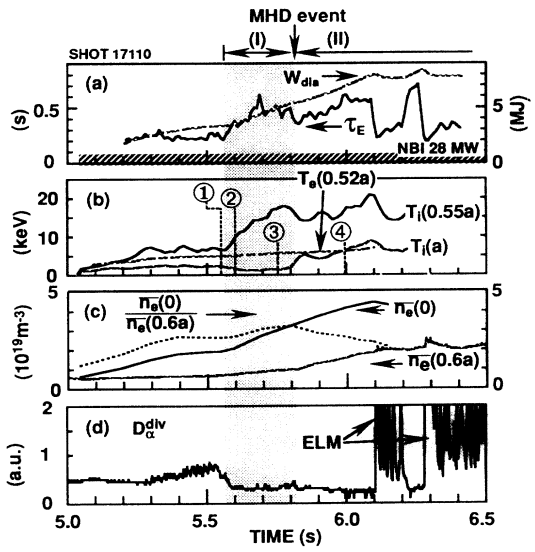

FIG. 1. Evolution of high-β_p H mode. (a) τ_E, global energy confinement time; W_{dia}, stored energy. (b) T_i, ion temperature at $r/a=0.55$ and $r/a=1$; T_e, electron temperature at $r/a=0.52$. Numbers 1-4 show time slices referred to in Fig. 2. (c) $\bar{n}_e$, line-average electron density measured along $r/a=0$ (tang. CO_2) and $r/a=0.6$ (vertical FIR); $\bar{n}_e(0)/\bar{n}_e(0.6a)$, density peaking factor. (d) D_α^{div}, deuterium-α emission from the divertor region.

0031-9007/94/72(23)/3662(4)$06.00

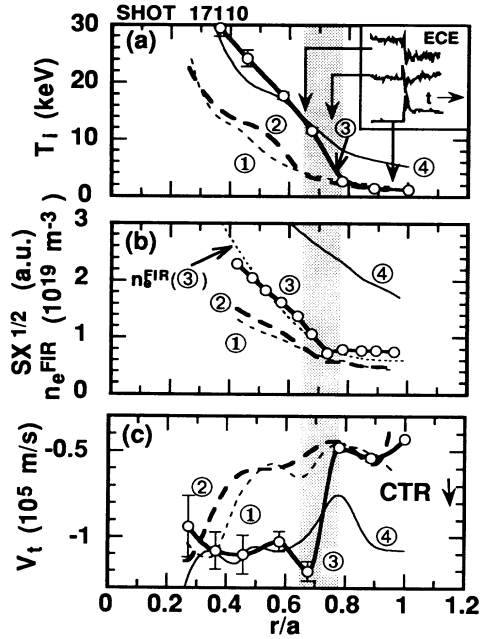

FIG. 2. (a) T_i, ion temperature profile. Numbers 1–4 are time slices shown in Fig. 1(b). The inset shows the traces of ECE signals. (b) The square root of the chord-integrated soft x-ray radiation profile. The dotted line shows the fitted $n_e(r)$ to the flux coordinate deduced from interferometers. (c) V_t, toroidal rotation velocity. The internal transport barrier location is shown with the shaded region.

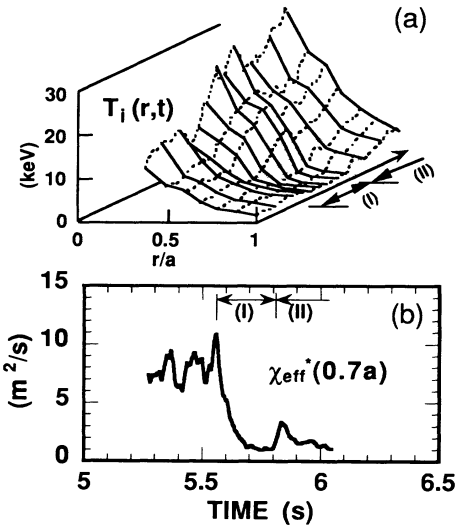

FIG. 3. (a) Time evolution of ion temperature. Shaded regions show the formation of internal and edge transport barriers. (b) Evolution of the effective thermal diffusivity χ_{eff}^*.

Here τ_E is defined as $W_{dia}/(P_t - dW_{dia}/dt)$ and P_t and W_{dia} are the total absorbed power and the plasma stored energy, respectively. At $t=5.05$ s, τ_E suddenly started rising to $2.5\tau_E^{ITER89\text{-}P}$. This was associated with the spontaneous increase in $T_i(0.55a)$ from 7 to 18 keV while the edge ion temperature $T_i(a)$ remained low (a is the volume-averaged minor radius). In this phase, identified as phase I and shown by the shaded region in Fig. 1, the density profile further peaked possibly due to the density buildup inside the $q=3$ surface. Phase I was terminated by a magnetohydrodynamic (MHD) crash localized near the $q=3$ surface at $t=5.81$ s. The edge ion temperature $T_i(a)$ jumped to 5 keV just after the MHD event and the density profile was gradually broadened. This phenomenon is similar to the sawtooth-induced H-mode transition in a tokamak although no clear D_α drop was seen in the D_α^{div} trace in Fig. 1. It is a remarkable contrast to the continuous increase in the edge ion temperature without transition in the hot ion H mode in JT-60U [10]. This plane, identified as phase II, is dubbed the "high-β_p H mode" [7]. The τ_E up to $3.6\tau_E^{ITER89\text{-}P}$ was achieved in phase II but the confinement was degraded by the appearance of the edge localized mode (ELM).

Figure 2(a) shows the evolution of the ion temperature profile. During the transition to phase I, a steep T_i gradient appeared at $r/a=0.6$. It moved to $r/a=0.7$ within 50 ms and stayed there for $\sim$150 ms, much longer than the temperature relaxation time $\tau_d \sim 1.5L_T^2/\chi_i$ of 12 ms; here L_T was defined as $T_i/(dT_i/dr)$ and was less than 0.1 m at the steep gradient region during phase I; χ_i is ion thermal diffusivity. Thus, a transport barrier with a reduced local thermal diffusivity was formed at $r/a=0.7$. The electron pressure profile, $P_e(r)=n_eT_e(r)$, inferred from the square root of the soft x-ray intensity (SX), also showed a steep gradient at $r/a=0.7$ [Fig. 2(b)]. This gradient came from a steep ∇n_e formed at $r/a=0.7$ since the change in the T_e profile was small as indicated in Fig. 1(b). The fitted $n_e(r)$ to the flux coordinate deduced from a tangential CO_2 and two vertical far infrared (FIR) interferometers is also shown in the same figure for comparison (the dotted line). The duration of phase I depends critically on the occurrence of the fast MHD event and has been extended stably to 500 ms in different discharges.

The "effective" single fluid thermal diffusivity, χ_{eff}^*, has been evaluated at $r/a=0.7$, where steep ∇T_i was formed in phase I (Fig. 3). Here the χ_{eff}^* is defined as

$$\chi_{eff}^* \equiv -Q_{eff} \Big/ \left(n_e \nabla T_e + \sum_i n_i \nabla T_i\right), \quad (1)$$

where $Q_{eff} \equiv (P_t - dW_{dia}/dt)/(4\pi^2 R_p 0.7a)$. The Q_{eff} is equivalent to the heat flux density across the $r/a=0.7$ surface, which includes both convective and conductive components, since 95% of both P_t and the plasma energy are contained with $r/a=0.7$ in phase I (85% in phase II). The effective thermal diffusivity $\chi_{eff}^*(0.7a)$ was reduced from 8 to 1 m^2/s at the transition to phase I. The decrease in χ_{eff}^* was mainly due to the change in ∇T_i since the change in ∇T_e was small. The steep ∇T_i was always accompanied by the strong sheared toroidal plasma rotation [Fig. 2(c)].

The location of the observed internal transport barrier was investigated for various discharge conditions. Figure 4 shows the q_{eff} dependence of the radial position of the

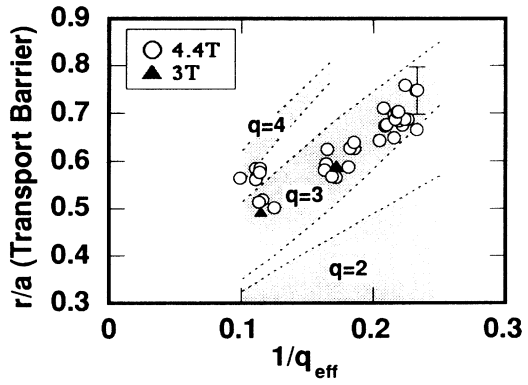

FIG. 4. The $q_{\rm eff}$ dependence of the radial position of the internal transport barrier. The shaded regions indicate the calculated radial positions of $q=2$, 3, and 4 surfaces with q_0 scanned over a range of 1.5–2.5. The vertical error bar is from the spatial resolution of the measurement.

internal transport barrier for both T_i and V_t. The data set contains the discharges that resulted in the transition to the high-β_p H mode or the loss of confinement after the fast MHD crash. Observed radial positions of the internal transport barrier were $r/a=0.7\pm0.05$ at $q_{\rm eff}=4$–5 and continuously shifted inward with increasing $q_{\rm eff}$. This clear $q_{\rm eff}$ dependence motivated us to investigate the radial location of internal transport barrier in connection with rational surfaces. The radial positions of $q=2$, 3, and 4 surfaces were calculated assuming the following current distribution:

$$j(r/a)=\frac{I_p}{\pi a^2}\frac{q_{\rm eff}}{q_0}\{1-(r/a)^2\}^{q_{\rm eff}/q_0-1}. \quad (2)$$

The bands in this figure indicate the range of results for the central safety factor, q_0, scanned over a range of 2 ± 0.5, which is consistent with the full MHD equilibrium fit and the absence of sawteeth. Almost all the data fell on the calculated location of the $q=3$ surface. Thus, the $q=3$ surface is the most likely explanation for the radial location of the internal transport barrier. Some data at $q_{\rm eff}\sim10$, however, deviate from the calculated location of the $q=3$ surface, which are left for a future study.

The following observation more convincingly supports the formation of the transport barrier near the $q=3$ surface. At the transition from phase I to phase II (indicated by "MHD event" in Fig. 1), a sudden release of energy across the internal transport barrier within 20 μs was detected with electron-cyclotron emission (ECE) measurement [Fig. 5(a) and the inset in Fig. 2(a)]. The fluctuation level of this crash was larger on the bad-curvature side [Fig. 5(b)]. This suggests that the pressure-driven MHD mode became unstable due to the pressure increase just inside the internal transport barrier and that this instability triggered the observed event. Magnetic fluctuations with a poloidal mode number $m=3$ were observed simultaneously as shown in Fig. 5(c). (The toroidal mode number was not identified due to the short duration

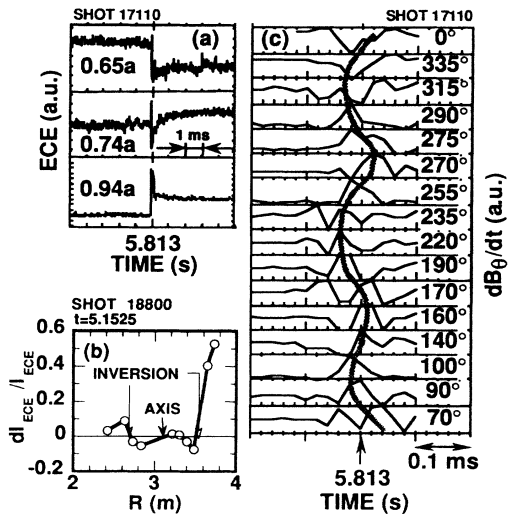

FIG. 5. (a) MHD event detected in ECE signals; (b) profile of fluctuation level; (c) MHD event detected in magnetic probe signals (numbers show poloidal angles of magnetic probes).

of the rapid crash.) This means that the inversion radius of the crash, i.e., the location of the internal transport barrier, was characterized by a resonant rational surface with $m=3$. Toroidal mode numbers of $n\geq2$ would correspond to $q\leq1.5$ at $r/a\sim0.7$ which is unlikely and $q=3$ with $n=1$ at $r/a\sim0.7$ is consistent with the results in Fig. 4.

The poloidal and toroidal plasma rotation in these discharges showed unique features. A large toroidal rotation shear or jump was observed across the $q=3$ surface as if momentum transfer across the internal transport barrier was significantly reduced in phase I as is shown in Fig. 2(c). The most striking feature was in the poloidal rotation velocity measurement at $r/a=0.8$ and $r/a=1$, as shown in Fig. 6. The impurity poloidal plasma rotation V_p at $r/a=0.8$ increased with time and reached -50 km/s in phase II. The value exceeded the neoclassical prediction [11] of -2.8 km/s by a factor of 18 and poloidal Mach number of impurity ions [$\equiv(B_t/B_p)(V_p/V_{\rm th})$; $V_{\rm th}$ is the thermal velocity of carbon ions] reached ~1. Since the radial position $r/a=0.8$ was $\sim17\sqrt{\varepsilon}\rho_p$ (ρ_p is the poloidal gyroradius of carbon ions) from the plasma surface, the poloidal torque due to ion orbit loss [12] should be negligibly small. Furthermore, the direction of V_p was opposite to the prediction based on the ion orbit loss and may suggest the loss of electrons. The improved theory [12] suggests a significant reduction of the parallel viscosity for a large poloidal Mach number. The improved theory for the impurity is needed to compare with this observation.

The radial electric field E_r is estimated from the lowest-order force-balance equation for the impurity,

$$E_r=V_tB_p-V_pB_t+\frac{1}{n_IZ_Ie}\nabla P_I, \quad (3)$$

where n_I, Z_I, e, P_I, B_t, and B_p are the impurity density,

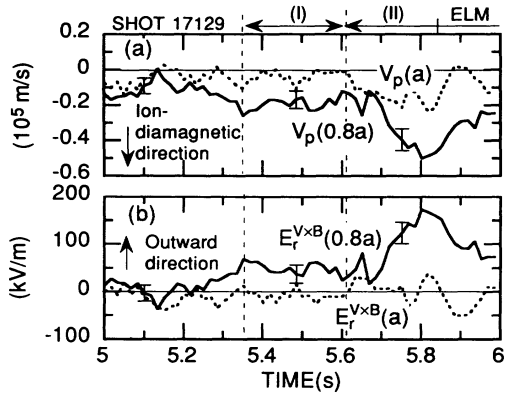

FIG. 6. (a) V_p, poloidal rotation velocity at $r/a=0.8$ and $r/a=1$; (b) radial electric field at $r/a=0.8$ and $r/a=1$ calculated from $-V\times B$ term in Eq. (3).

the ionic charge of the impurity, the electric charge, the impurity ion pressure, and the toroidal and poloidal magnetic fields, respectively. We estimated only the $-V\times B$ term in Eq. (3) ($\equiv E_r^{V\times B}$) because the contribution of the ∇P_I term was sufficiently small ($|\nabla P_I/n_I Z_I e| \leq 10$ kV/m) compared with the $-V\times B$ term ($|V\times B|\sim 100$ kV/m) at $r/a=0.8$ and because we have no detailed measurement of ∇P_I at $r/a\sim 1$.

Figure 6(b) shows a large positive $E_r^{V\times B}$ at $r/a=0.8$ due to the larger positive contribution from $V_p B_t$ compared with the negative $V_t B_p$ term (at $r/a=0.8$–1, B_t was larger than B_p by a factor of 6–7). The $E\times B$ velocity shear, $d(E_r/B)/dr$, built up in phase II since $E_r^{V\times B}(0.8a)$, increased from 40 to 170 kV/m while $E_r^{V\times B}(a)$ remained unchanged. An inclusion of the possible substantial contribution of the ∇P_I term due to the edge transport barrier gives a more negative E_r at $r/a\sim 1$ and results in a larger $E\times B$ velocity shear. However, the role of this $E\times B$ velocity shear in the confinement improvement remains an unresolved question.

In summary, we observed spontaneous formation of an internal transport barrier near the $q=3$ surface in JT-60U high-β_p discharges. The confinement improvement propagated outward and stagnated at the $q=3$ rational surface, suggesting a special role for the rational surface on the transport process in a tokamak. It has been recognized that special flux surfaces can play an important role in the improved confinement such as the outermost closed flux surface in the H mode [13] and the $q=1$ surface in the pellet-induced improved confinement regime [14]. Since Mercier stability properties change across the $q=1$ surface, the $q=1$ surface has been thought to be different from other rational surfaces in a tokamak. Our observation indicates that the transport barrier could be formed in any rational surface. We reported also the appearance of a poloidal plasma rotation velocity that greatly exceeded the present-day neoclassical prediction at $\sim 17\times\sqrt{\varepsilon}\rho_p$ from the plasma surface. The poloidal plasma rotation in a tokamak has been believed to be strongly damped due to a large neoclassical parallel viscous force except at the very edge [12]. Previous measurements [15,16], consistent with the theoretical prediction, showed very small poloidal plasma rotation except at the edge. The experimental observations of the bootstrap current also indicated the existence of this parallel viscous force [17]. However, our observation clearly showed that at least the impurity can rotate very rapidly (or spin up) in the poloidal direction indicating the reduced parallel viscous force in the plasma interior.

The authors express thanks to Dr. Y. Miura, Dr. M. Azumi, Dr. M. Nagami, Dr. H. Ninomiya, Dr. H. Kishimoto (JAERI), Dr. K. Ida (National Institute for Fusion Science), Dr. M. Yamada, and Dr. H. Park (Princeton University) for their beneficial comments. The assistance from Professor H. Sugai (Nagoya University) and the DIII-D group (General Atomics) on boronization and from the TFTR group on the physics of high-β_p discharges was very helpful for the experiments.

[1] M. Kikuchi, Nucl. Fusion **30**, 265 (1990).
[2] Y. Seki *et al.*, in *Proceedings of the Thirteenth International Conference on Plasma Physics and Controlled Nuclear Fusion Research, Washington, D.C., 1990* (IAEA, Vienna, 1991), Vol. 3, p. 473; R. W. Conn, *et al.*, *ibid.*, Vol. 3, p. 659.
[3] P. N. Yushmanov *et al.*, Nucl. Fusion **30**, 1999 (1990).
[4] M. Kikuchi, Plasma Phys. Controlled Fusion **35**, 39 (1993).
[5] S. Ishida *et al.*, in *Proceedings of the Fourteenth International Conference on Plasma Physics and Controlled Nuclear Fusion Research, Würzburg, 1992* (IAEA, Vienna, 1993), Vol. 1, p. 219.
[6] T. N. Todd, in *Proceedings of the 2nd European Tokamak Programme Workshop, Sault-Les-Chartreux, 1983* (European Physical Society, Petit-Lancy, Switzerland, 1983), p. 123.
[7] M. Mori *et al.* (to be published).
[8] T. Nishitani *et al.* (to be published).
[9] M. Saidoh *et al.*, Jpn. J. Appl. Phys. **32**, 3276 (1993); J. Winter *et al.*, J. Nucl. Mater. **162–164**, 713 (1989).
[10] M. Kikuchi *et al.*, in *Proceedings of the 20th European Conference on Controlled Fusion and Plasma Physics, Lisboa, 1993* (European Physical Society, Petit-Lancy, Switzerland, 1993), Part 1, p. 179.
[11] Y. B. Kim *et al.*, Phys. Fluids B **3**, 2050 (1991).
[12] K. C. Shaing *et al.*, Phys. Rev. Lett. **63**, 2369 (1989).
[13] F. Wagner *et al.*, Phys. Rev. Lett. **53**, 1453 (1984).
[14] Y. Kamada *et al.*, Nucl. Fusion **31**, 23 (1991).
[15] K. H. Burrell *et al.*, Plasma Phys. Controlled Fusion **34**, 1859 (1992).
[16] K. Ida *et al.*, Phys. Rev. Lett. **65**, 1364 (1990).
[17] M. C. Zarnstorff *et al.*, Phys. Rev. Lett. **60**, 1306 (1988).

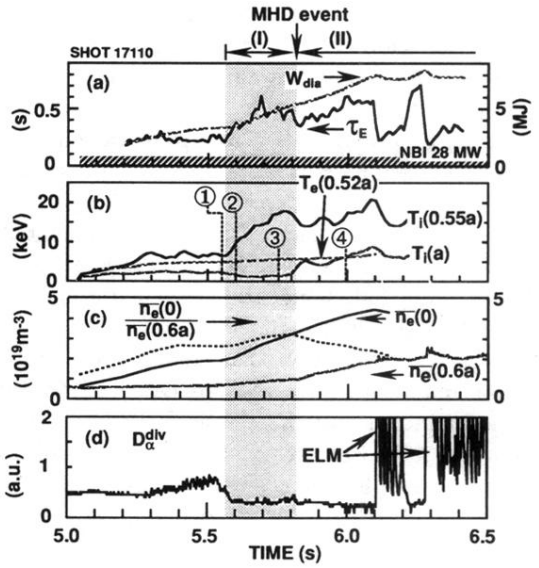

FIG. 1. Evolution of high-β_p H mode. (a) τ_E, global energy confinement time; W_{dia}, stored energy. (b) T_i, ion temperature at $r/a=0.55$ and $r/a=1$; T_e, electron temperature at $r/a=0.52$. Numbers 1–4 show time slices referred to in Fig. 2. (c) $\bar{n}_e$, line-average electron density measured along $r/a=0$ (tang. CO_2) and $r/a=0.6$ (vertical FIR); $\bar{n}_e(0)/\bar{n}_e(0.6a)$, density peaking factor. (d) D_α^{div}, deuterium-α emission from the divertor region.

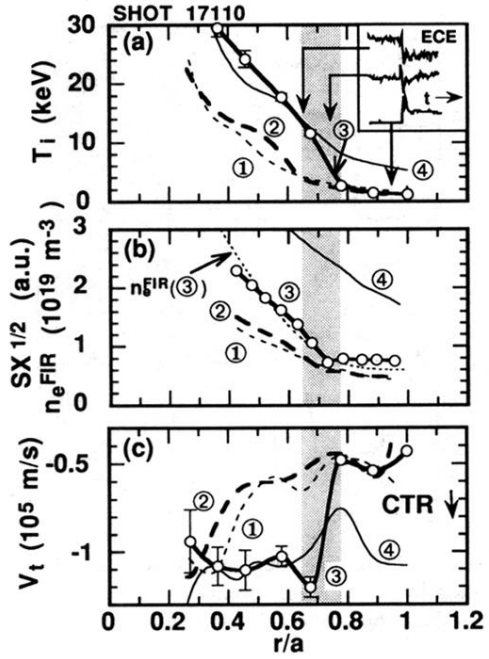

FIG. 2. (a) T_i, ion temperature profile. Numbers 1–4 are time slices shown in Fig. 1(b). The inset shows the traces of ECE signals. (b) The square root of the chord-integrated soft x-ray radiation profile. The dotted line shows the fitted $n_e(r)$ to the flux coordinate deduced from interferometers. (c) V_t, toroidal rotation velocity. The internal transport barrier location is shown with the shaded region.

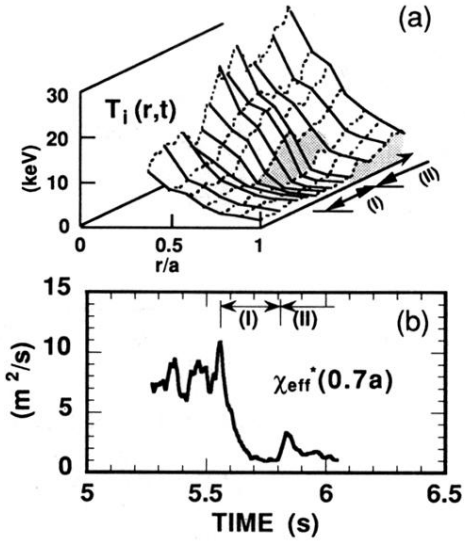

FIG. 3. (a) Time evolution of ion temperature. Shaded regions show the formation of internal and edge transport barriers. (b) Evolution of the effective thermal diffusivity χ_{eff}^*.

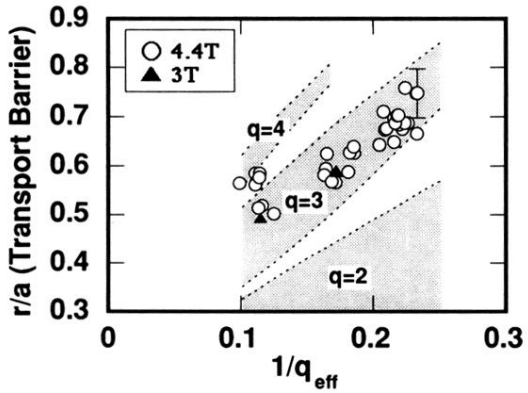

FIG. 4. The q_{eff} dependence of the radial position of the internal transport barrier. The shaded regions indicate the calculated radial positions of $q=2$, 3, and 4 surfaces with q_0 scanned over a range of 1.5–2.5. The vertical error bar is from the spatial resolution of the measurement.